

# A parameter refinement method for Ptychography based on Deep Learning concepts

Francesco Guzzi<sup>1,2,\*</sup>, George Kourousias<sup>2</sup>, Fulvio Billè<sup>2</sup>, Roberto Pugliese<sup>2</sup>, Alessandra Gianoncelli<sup>2</sup>, and Sergio Carrato<sup>1</sup>

<sup>1</sup>Image Processing Laboratory (IPL), University of Trieste, Italy

<sup>2</sup>Elettra Sincrotrone Trieste, Italy

\*francesco.guzzi@elettra.eu

## ABSTRACT

X-ray Ptychography is an advanced computational microscopy technique which is delivering exceptionally detailed quantitative imaging of biological and nanotechnology specimens. However coarse parametrisation in propagation distance, position errors and partial coherence frequently menaces the experiment viability. In this work we formally introduced these actors, solving the whole reconstruction as an optimisation problem. A modern Deep Learning framework is used to correct autonomously the setup incoherences, thus improving the quality of a ptychography reconstruction. Automatic procedures are indeed crucial to reduce the time for a reliable analysis, which has a significant impact on all the fields that use this kind of microscopy. We implemented our algorithm in our software framework, SciComPty, releasing it as open-source. We tested our system on both synthetic datasets and also on real data acquired at the TwinMic beamline of the Elettra synchrotron facility.

## 1 Introduction

X-ray transmission microscopy is a vast family of techniques that aim at investigating the microscopic nature of thin, non-crystalline materials, essentially by illuminating the sample and observing how it modulates the input wavefield. If contact imaging leads to images without diffraction ringing<sup>1</sup>, on the other hand, the lack of phase information is critical for biological specimens. Research on lens-less Coherent Diffraction Imaging (CDI) methods led to transmission ptychography<sup>2</sup>, an advanced technique that provides high-resolution phase imaging of large specimens. Ptychography and CDI involve *inverse problems*, meaning that from the set of measured quantities (diffraction patterns) we want to step back to the cause that originated them<sup>3,4</sup>; as microscopists, we are interested in retrieving the structure of the object, expressed as a two-dimensional transmission function  $O(x,y)$ .

Being severely ill-posed<sup>5</sup>, an iterative phase retrieval procedure is employed to find a solution. An *a priori* image formation model is used to *simulate* the experiment, by producing synthetic quantities which depend on the current estimate of the latent variables (e.g.  $O(x,y)$ ); it is the comparison between simulated and measured quantities (an *error function*) that guides the solution. Many modern algorithms are formalised following the Projection Over Set (POS) approach, defined by sequentially applying different constraints on the solution estimate<sup>3,6</sup>, effectively leading it towards the intersection of each constraints set. CDI techniques (and thus ptychography) are extremely sensitive to a coarse parameter estimation<sup>3,7,8</sup>, and this may result in a severely degraded reconstruction. While projection-based methods are easy to design and implement, automatic correction of setup parameters cannot be formally introduced: a long trial and error procedure is typically employed to manually refine these quantities, looking for the output with fewer artefacts. On the contrary, framing the reconstruction as a gradient-based optimisation process, the loss function can be written with an explicit dependency of the model parameters, for which an update function can be calculated. As the model complexity increases, the gradient expressions becomes progressively more difficult to calculate, and indeed Automatic Differentiation (AD) methods (also referred as "autograd")<sup>9,10</sup> applied to ptychography are recently getting lots of attention as an effective way to design complex algorithms<sup>11,12</sup>.

In the present work, a novel AD-based ptychography reconstruction algorithm is presented. Exploiting the capabilities of the modern Deep Learning (DL) tools, a loss function is derived by explicitly taking into account the setup parameters, which are added to the optimisation pool for a joint regression-reconstruction. We independently followed the same general idea of<sup>12</sup> but: I) an angular spectrum<sup>13</sup> propagation model is implemented in place of the Fresnel approximation<sup>14</sup>; the robustness of the algorithm is greatly increased by including II) a position refinement routine, III) the propagation distance regression and IV) the illumination decomposition. To the best of our knowledge, no attempts in the literature have been made to cope with these problems, not only as a whole but also in the frame of differentiable programming algorithms, then improving the technique. The software is released as open-source (upon publication<sup>15</sup>).

This paper is organized as follows: in section 2 we provide a brief introduction on the ptychography forward model, defining the major flaws we want to correct, as well as a brief description of the autograd technology. In section 3, our computational methodology is described, introducing the designed loss function and the Spatial Transform components. In section 4 we present our main results, while section 5 concludes the paper.

## 2 Background

Ptychography<sup>16–18</sup> (Fig. 1) is a hybrid scanning - CDI technique, in which a single extended object is illuminated with a disk of light that sequentially scans multiple areas of the same specimen; the intensity of the resulting scattered wave is recorded by a detector placed at some distance. This configuration allows for a large field of view to be acquired, conversely to CDI<sup>2</sup>. By illuminating adjacent areas with a high overlap factor, redundancy is introduced in the acquisition, thus creating a robust set of constraints which greatly improve the convergence of the phase-retrieval procedure<sup>6</sup>. If the set of diffraction patterns is properly recorded (e.g. assumptions in<sup>19</sup> hold) and the entire experimental framework is coherent with the measured data (eq. 1 is a valid model), the reconstruction algorithm converges to a stable solution, providing a meaningful reconstruction of  $O(\mathbf{r})$  at a resolution which in principle is also higher than the Abbe diffraction limit<sup>20</sup>.

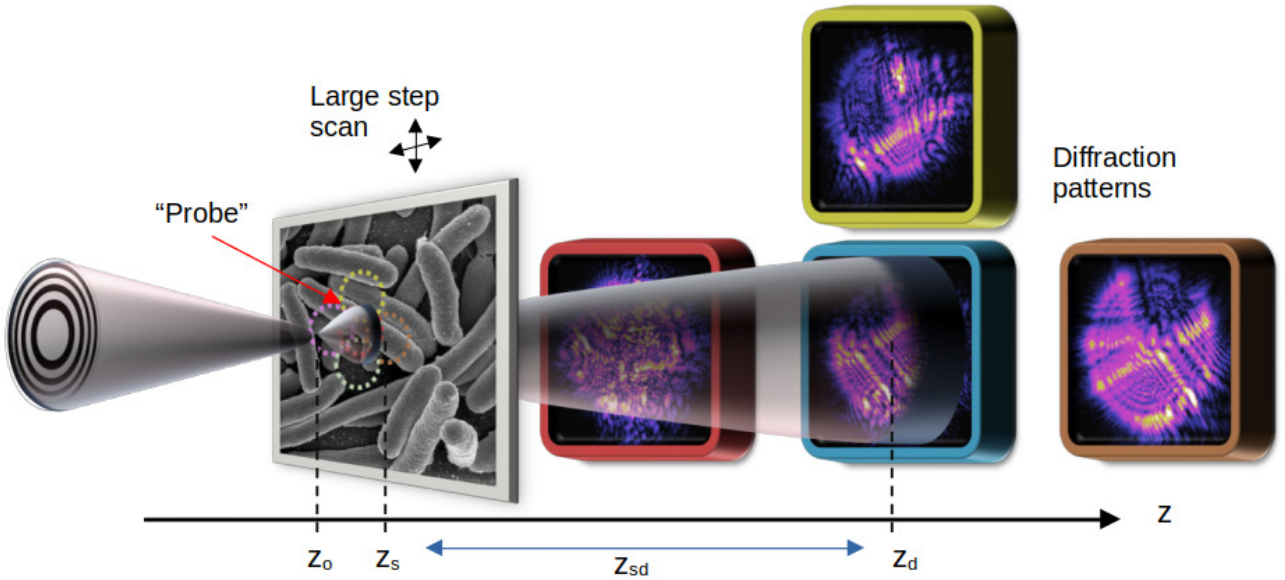


**Figure 1.** A typical ptychography setup used in synchrotron laboratories: a virtual point source illuminates (probe) a well-defined region on the sample, which is mounted on a motorized stage. The scattered field intensity is recorded at a distance  $z_d$ .

### 2.1 Ptychography model

A ptychography dataset is composed by a set of diffraction patterns  $I_j$  with  $j \in [1, \dots, J]$ , each singularly being the outcome of an independent CDI experiment, performed onto a region of the sample. The image formation model can be described by the following expression:

$$I_j(\mathbf{r}) = |D_z\{P(\mathbf{r})O_j(\mathbf{r}_j)\}|^2, \quad (1)$$

where  $P(\mathbf{r})$  is the 2D illumination on the sample plane (coordinates  $\mathbf{r}$ ) and  $O_j(\mathbf{r}_j)$  is the 2D transmission function of the sample in the local reference system  $\mathbf{r}_j$ , centred at the known  $j$ th scan position.  $D_z$  is an operator which describe the observation of the pattern at a known distance  $z$ . Knowing the illumination onto a region of the object is crucial for the factorisation of the exit wave  $P(\mathbf{r})O_j(\mathbf{r}_j)$ , and in the typical CDI experiment, it must be provided as a piece of *a priori* information. In a modern ptychography reconstruction, instead, the illumination function (both in magnitude and phase) is a free (but necessary) by-product of the process obtainable thanks to redundancy in the dataset<sup>21,22</sup>: the so-called "probe retrieval" procedure can also reconstruct a multi-mode illumination, which is a well-known model to describe the partial coherence of a third-generation light source<sup>23–26</sup>. In order to take into account the independent propagation of  $M$  mutually-incoherent probes, equation (1) is

modified in the following manner:

$$I_j(\mathbf{r}) = \sum_{p=1}^M |D_z\{P_p(\mathbf{r}) \cdot O(\mathbf{r}_j)\}|^2, \quad (2)$$

where the exit wave produced by the modulation of each  $P_p(\mathbf{r})$  mode is summed in intensity on the observation plane.

## 2.2 Parameters refinement

We can denote as "setup incoherences" all the deviations of a real setup from the a priori model defined in equation (1). Partial coherence, energy spread, position error and distance errors are common and severe sources of artefacts in a ptychography reconstruction. Browsing through the ptychography corpus, it appears that the majority of the attention in automatic correction is devoted mainly to the first three flaws; partial coherence and mixed state ptychography has been extensively reviewed in the literature (e.g. in<sup>6,27,28</sup>), while only in<sup>8</sup> an evolutionary algorithm is used to cope with the uncertainty on the source-to-sample distance in electron ptychography, that translates in a spherical aberration of the probe; in the context of<sup>8</sup> (electron ptychography), indeed, conventional probe-solving algorithms like EPIE<sup>29</sup> and DM<sup>22</sup> would fail<sup>8</sup> then, the reconstruction is carried out just using the conventional PIE algorithm<sup>29</sup> which requires a well-defined a-priori probe function. In<sup>30</sup> the authors propose to use a position refinement scheme also to correct for the axial parameters, as the latter is responsible to modifying the distances between adjacent probes, while in the very recent (January 2021) work<sup>31</sup>, the authors use an autograd environment to infer directly the propagation distance, but the resulting method is tested on visible light only. Fig. 2 (panel A) shows the effect of a wrong propagation distance estimate on the retrieved probe: speckle-like patterns typically appears.

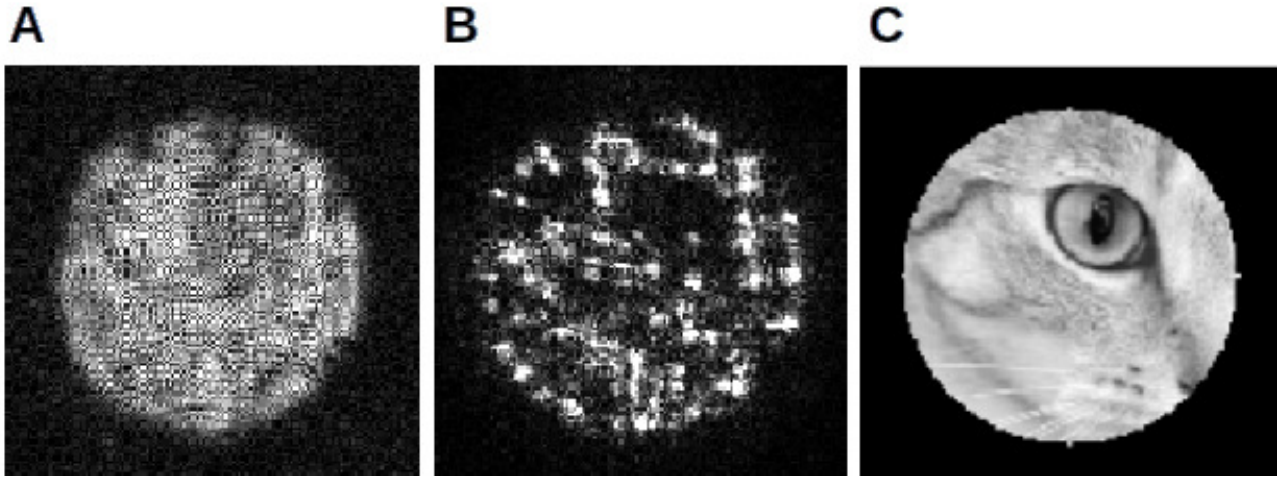


**Figure 2.** Typical artefacts in a probe retrieval procedure (simulated data) in the case of wrong propagation distance (panel A, speckle patterns) and no position refinement (panel B, cluster of dots) Panel C shows the real illumination (magnitude).

In many ptychography setups, the positions list of the scan is typically directly taken from the commands that the control system sends to the sample stage<sup>3</sup>; the final movement is composed using a servo for the coarse step and a piezo for the fine shifts. Even a minor misalignment (wrong positions) within the order of magnitude of the desired resolution, caused e.g. by non-linear thermal-drift induced deformations or motor backlash, can lead to severe degradation of the reconstruction<sup>7</sup>. This is a natural characteristic of any computational imaging technique based on some sort of movement, and in fact applies e.g. to super-resolution imaging<sup>32</sup>. Indeed, as can be seen in Fig. 3, the effects of the errors are quite disruptive, especially due to the fact that the entire object computational box changes format. Cluster of dots in the retrieved probe (Fig. 2, panel B), are a typical symptom of wrong positions.

Positions refinement in ptychography has been historically treated as non-linear optimisation process which takes into account the object and the positions, such as in<sup>33</sup>, however without regularisation this approach can easily lead to local minima. A second important limitation of the method lies in the huge computational cost associated to adjunct DFTs required to describe the space-shift operators. To cope with this problem, numerous solutions have been proposed by combining a conventional reconstruction algorithm such as EPIE<sup>29</sup>, ML<sup>34</sup>, DM<sup>22</sup> with an optimisation based positions correction routine. For example, in the work<sup>35</sup>, the correction is carried out within a gradient-less approach using the Powell method<sup>36</sup>, while in<sup>37</sup> the optimisation provided by<sup>33</sup> is used. In<sup>21</sup> an annealing algorithm is exploited, essentially by exhaustively exploring the shifts parameter

space and using the diffraction re-projection error metric as a reference; a similar approach is defined in<sup>38</sup>, highlighting the use of the Structural Similarity Index<sup>39</sup> as a more suitable metrics. Unfortunately, methods of this type are for their nature computationally expensive. In<sup>40</sup>, a finite-difference approximate but fast update step is employed. More promising methods use instead a position error signal which can be estimated by a cross-correlation procedure, such as in<sup>41</sup>. In<sup>3</sup> the error signal dynamics is studied and an acceleration is provided by employing the Adam algorithm<sup>42</sup>. The same concept of re-projections is currently applied also in a tomography environment (e.g in<sup>43</sup>).

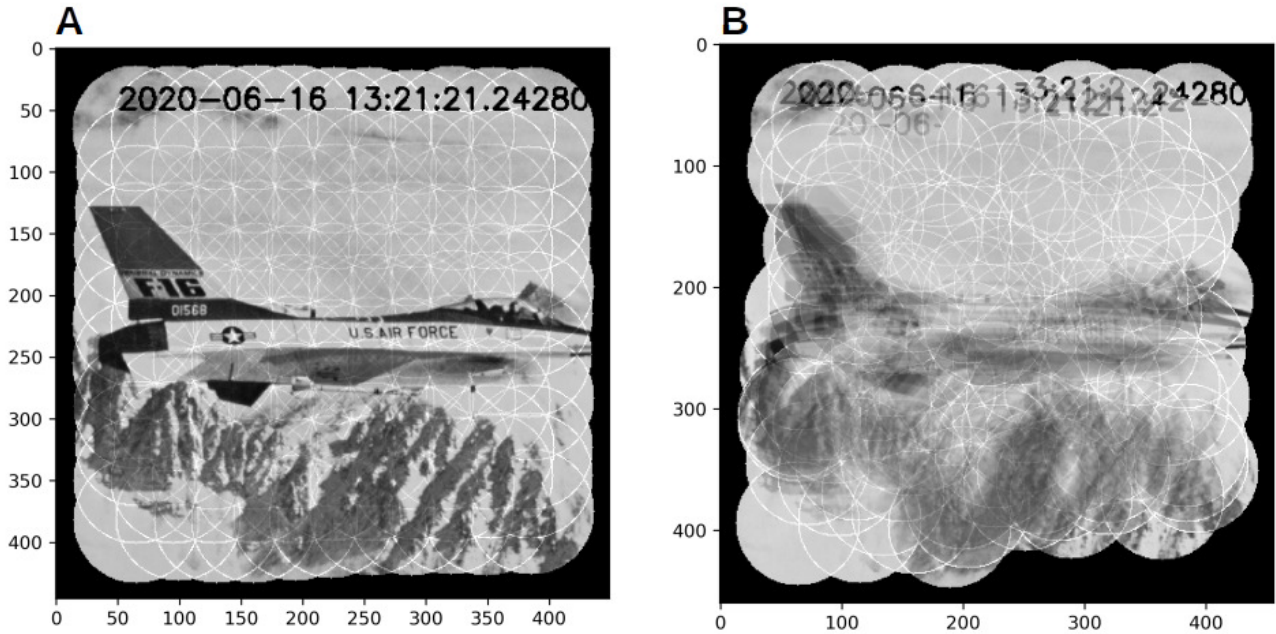


**Figure 3.** Artificial stitching of the illuminated object ROIs with correct (panel A) and wrong positions (panel B): severe artefacts are produced together with a deformation of the total computational box (maximal occupation).

### 2.3 Automatic Differentiation

An unconstrained optimisation problem aims at minimise a real-valued *objective function*  $f(\mathbf{x})$  (loss, cost) of  $N$  variables. This problem can be formally expressed by the following expression:

$$\tilde{\mathbf{x}} = \underset{\mathbf{x}}{\operatorname{argmin}} f(\mathbf{x}), \quad (3)$$

where  $\tilde{\mathbf{x}}$  is the sought  $N$ -vector solution. One of the common methods to iteratively minimise the function  $f(\mathbf{x})$  is the *gradient descent* procedure, which relies on the gradient of the objective function to define an update step:

$$\mathbf{x}_{k+1} = \mathbf{x}_k - \alpha \nabla_{\mathbf{x}} f(\mathbf{x})|_{\mathbf{x}=\mathbf{x}_k} \quad (4)$$

that will provide a new vector estimate  $\mathbf{x}_{k+1}$  from the previous estimate  $\mathbf{x}_k$ , which at the convergence will be equal to  $\tilde{\mathbf{x}}$ . Handmade symbolic computation of  $\nabla_{\mathbf{x}} f(\mathbf{x})$  becomes increasingly tedious and error-prone as the complexity of the expression increases. Numerical differentiation provides automatically an estimate of the point derivative of a function by exploiting the central difference scheme but, while this method is particularly effective for few dimensions, it becomes progressively slow as  $N$  rises. On the other side, a Computer Algebra System (CAS) generates a symbolic expression through *symbolic computation*, but often the output results in *expression swell*. Automatic Differentiation<sup>44–46</sup> is a way to provide an accurate gradient calculated at a point, thus lying in between numerical differentiation and handmade calculation. In one of the currently used methods to compute automatically the gradients<sup>47</sup>, when a mathematical expression is evaluated, each temporary result constitutes a node in a computational acyclic graph that records the story of the expression, from the input variables to the generated result. The gradient is simply calculated following backwards the graph (backward mode differentiation<sup>46</sup>), from the results to the input variables, just applying the chain rule to the gradient of each nuclear differentiable operator<sup>44</sup> ("operator overloading" mechanism<sup>45,46</sup>). To do so, each object (tensor) contains, indeed, not only the actual data but also i) the handler to the last operation that produced that variable, and ii) a second data array containing the gradient. This particular data type is called *doublet* in the literature<sup>44</sup>.



### 3 Computational Methodology

Ptychography forward model is defined in terms of a complex probe vector  $\mathbf{P} \in C^K$  interacting with a complex object transmission function which can also be arranged as a vector  $\mathbf{O} \in C^D$ .

#### 3.1 Loss Function

Loss functions are typically designed around simple metrics such as quadratic norms, which can be real functions of a complex variable. When all the conditions defined in section 2 hold, a loss function  $\mathcal{L}$  for all the  $j \in [1 \dots N]$  diffraction patterns and positions in the dataset can be written as a *data fidelity term*:

$$\mathcal{L}(\mathbf{P}, \mathbf{O}, z) = \sum_{j=1}^N \left\| \tilde{I}_j(\mathbf{P}, \mathbf{O}, z) - \sqrt{I_j} \right\|^2. \quad (5)$$

As it can be seen, (5) is a function of the  $2K + 2D + 1$  real variables which stacked up constitute the optimisation vector pool. The simulated diffraction pattern  $\tilde{I}_j$  relative to the current  $j$ th computational box is calculated by (1) or by its extension to a multi-mode illumination (2). The square root of the recorded data can be computed once for all the diffractions to fasten the implementation.  $D_z$  is the angular spectrum propagator<sup>48</sup> defined by the expression:

$$\Psi_o(x, y; z - z_i) = \mathcal{F}^{-1} \{ \mathcal{F} \{ \Psi_i(x, y; z_i) \} \cdot \mathcal{F} \{ h(x, y, z) \} \}, \quad (6)$$

which relates the input field  $\Psi_i$  to the output field at the detector plane  $\Psi_o$ . Fixing the wavelength  $\lambda$  of the incident radiation, the 2D Fourier transform of the propagation filter  $h$  is defined by:

$$\mathcal{F} \{ h(x, y, z) \} = H(f_x, f_y, z) = e^{jkz \cdot \sqrt{1 - (\lambda f_x)^2 - (\lambda f_y)^2}}. \quad (7)$$

Current DL autograd tools are not conceived to work with complex number, then a basic complex library needs to be written; the natural way to introduce them is to just add an extra dimension to each 2D tensor and incorporate the real and the imaginary part in the same object, basically duplicating the number of actual variables. Automatic backward operation is completely legit for this kind of custom-made datatype and the resulting gradient is simply:

$$\text{grad } f(\mathbf{x}) = 2\nabla_{\mathbf{x}^*} f(\mathbf{x}) = \frac{\partial f}{\partial \mathbf{x}^*} = \left( \frac{\partial f}{\partial \mathbf{a}} + j \frac{\partial f}{\partial \mathbf{b}} \right) \quad (8)$$

where  $\mathbf{x} = \mathbf{a} + j\mathbf{b}$ . The actual gradient is represented in the same complex data type of the variables, made of a real and an imaginary part. As can be seen in (8), the result of the automatic differentiation can be written in the Wirtinger formalism<sup>49</sup> just as the derivative with respect to the conjugate of the differentiation variable (except for the constant), that is the typical gradient expression exploited for functions of complex variables.

To increase the quality of the reconstruction, the data fidelity term in a loss function is usually paired with a regularisation term (method of the Lagrange Multipliers), whose role is to penalise *ad hoc* solutions in the parameters space: a pixel value ought to fit the physical nature of the beneath model, without just accommodating the dissimilarity measure; this translates into a mere energy-conservation constraint.

#### 3.2 Spatial Transform layer

If as seen in (5) and (6) writing a mathematical expression in the parameters  $\mathbf{O}$ ,  $\mathbf{P}$  and  $z$  directly permit the gradient generation, the same does not hold for the spatial shift correction defined onto a discrete sampling grid. Indeed, in the typical ptychography reconstruction algorithm, the computational box for a given  $j$ th position is defined exploiting a simple crop operator on a 2D tensor. While this method is simple and computationally fast (pointer arithmetics), it is not differentiable, as integer differentiation is nonsense. In this work, an approach borrowed from the DL community is then explored.

Convolutional neural networks are not invariant to geometric transforms applied to their input. To cope with this problem, a Spatial Transform layer<sup>50</sup> is introduced; the new learnable model is trained at inferring the spatial transformation that, applied to the an input feature map, maximises the task metric. This approach greatly improves classification and recognition performances (e.g. in face recognition<sup>51</sup>).

In this work the parameters of the affine transform are directly learned as the position refinement coefficients which minimise the objective function (5) during the reconstruction. To do so, two components are used: (i) a grid generator and (ii) a grid sampler. The first element transforms a regular input sampling grid  $(x_i, y_i)^T$  in an output coordinates grid  $(x_o, y_o)^T$ , by applying an affine transform to the former; this mapping (9) is fully defined by 6 degrees of freedom, but for what concerns rigid

translation, only the last column  $(t_x, t_y)^T$  is optimised. The scaling factors  $(s_x, s_y)^T$  are thus constants used to crop the central region.

$$\begin{pmatrix} x_o \\ y_o \end{pmatrix}_j = \begin{pmatrix} s_x & 0 & t_x \\ 0 & s_y & t_y \end{pmatrix}_j \begin{pmatrix} x_i \\ y_i \end{pmatrix}_j \quad (9)$$

Then for each  $j$ th diffraction pattern and each  $j$ th shift-vector  $(t_x, t_y)^T$  the  $j$ th output grid  $(x_o, y_o)^T$  is generated. From the latter, the grid sampler thus outputs a warped version of the object. Following the formalism introduced in<sup>50</sup>, the cropped portion of the object  $V_j$  is generated from the entire object  $U$  by:

$$V_j = \sum_{h=1}^H \sum_{w=1}^W U_{w,h} \cdot k(w - x_j, h - y_j) \quad (10)$$

A well-done sampling (with an anti-aliasing filter) adds a regularisation term that can help during the optimisation. The bilinear sampling exploits a triangular (separable) kernel  $K$ , defined in (11) which does not present dangerous overshooting artefacts:

$$K(w - x, h - y) = K_1(w - x) \cdot K_1(h - y) \quad (11)$$

where

$$K_1(t) = \max(0, 1 - |t|) \quad (12)$$

Fig. 4 shows the structure of the proposed approach, applied to the Ptychography framework. The same spatial transform is enforced on the two channels of the tensor that represent real and imaginary parts of the cropped region of the object. Within this setup, gradient propagation is possible because derivative expressions can be calculated with respect to both the affine grid and the output pixel values<sup>50</sup>.

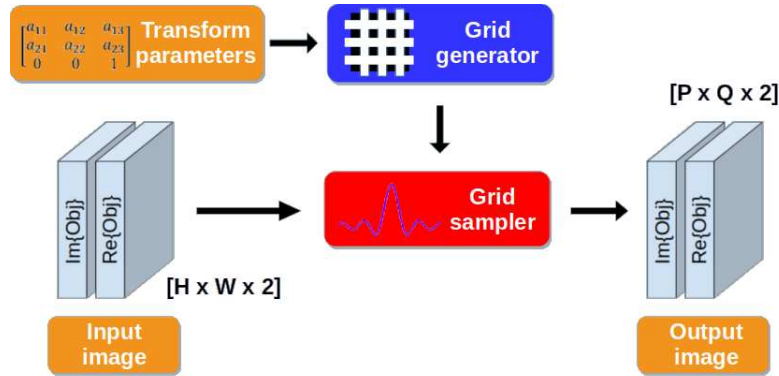


**Figure 4.** Schematics of the differentiable components used in our method. For each positions vector, a grid generator takes as input the corresponding shift transform expressed in an affine transform formalism; the sampling grid is then generated using this information. The object is then sampled at each coordinate defined by the sampling grid, producing the correct cropped region of the object.

## 4 Results and discussion

A Ptychography simulator, implemented in the SciComPty modular framework<sup>3</sup>, is used to create 5 synthetic datasets, starting from a set of standard test images and setup parameters which spans different propagation distances, from 0.065 m to 0.2 m. All the computational experiments are written on PyTorch 1.2<sup>47</sup> and executed on a computer equipped with an Intel Xeon (R) E3-1245 v5 CPU running at 3.50 GHz. The entire code is implemented on GPU (Nvidia Quadro P2000), which is essential for this heavy-duty computational imaging. During the tests on synthetic data, the resolution for each diffraction pattern is limited to 128x128 pixels to reduce the computation time. The overlap factor is kept constant at around 70%, producing a scan pattern of 11x11 positions. A known random jitter is added to the ideal grid-based scan pattern to avoid the "raster scan pathology"<sup>22</sup>. The resulting total object size has a field of view of around 512x512 pixels. Within the context of this paper, the term "epoch",

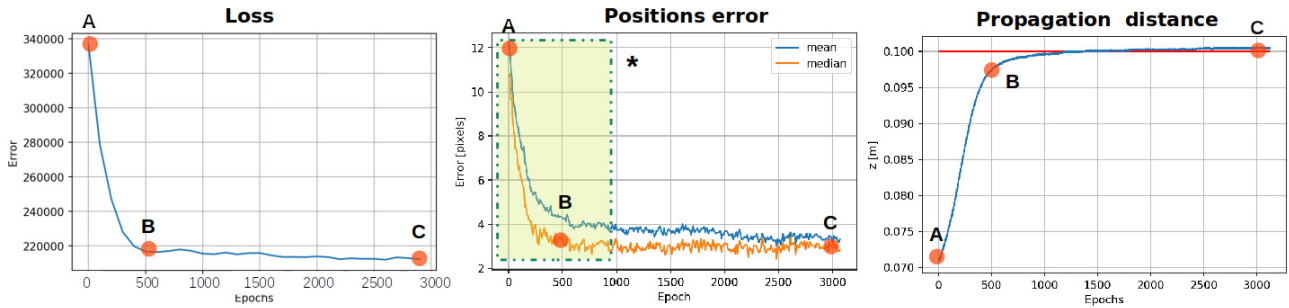


**Figure 5.** The convergence of our combined optimisation is analysed by observing: the dissimilarity error(left), the ground truth position error (center) and the propagation distance inferred by the algorithm (right). In the leftmost panel, the correct distance is denoted by the red horizontal line at  $z = 0.1\text{m}$

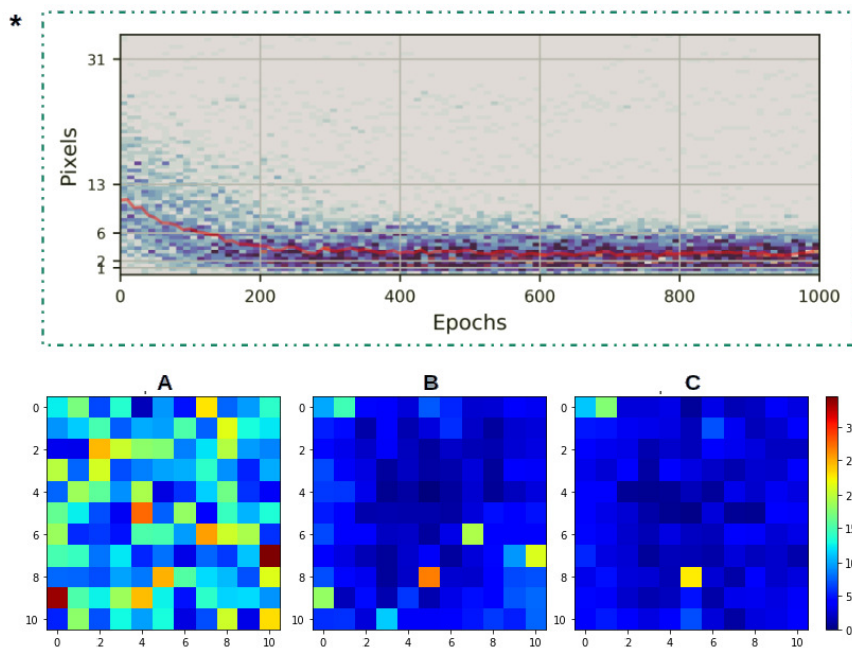


**Figure 6.** The uppermost graph is the zoomed version of the central panel in Fig. 5 (denoted by an asterisk). Here, the distribution of the positions errors is shown as epochs increase. It can be seen that the median decay towards 0 as the reconstruction proceeds. Panel A,B and C shows the ground truth error for each of the 11x11 positions.

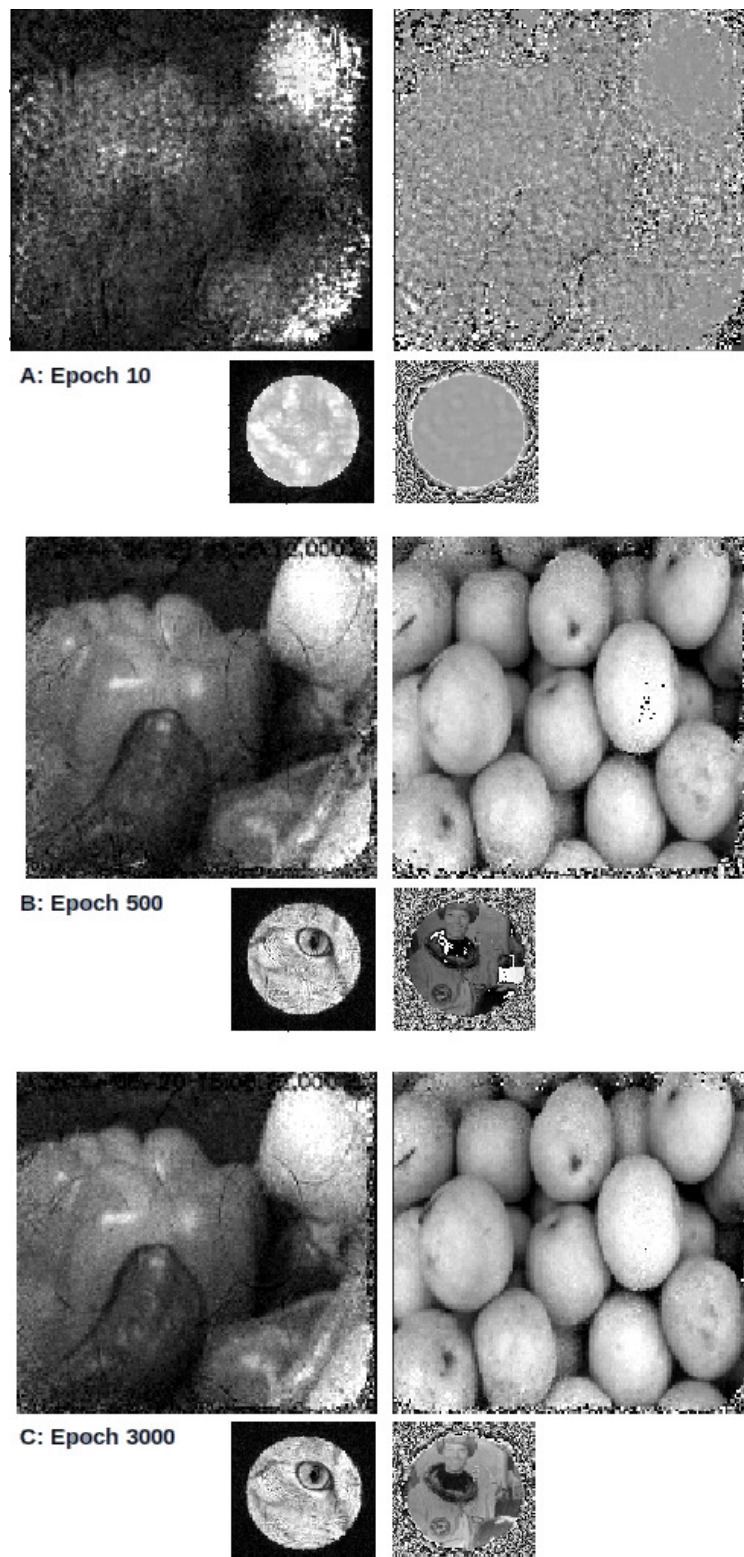


**Figure 7.** Evolution of the reconstruction for a synthetic dataset, shown at the epoch denoted by A, B and C in Fig. 5.

which is used interchangeably with "iteration", defines how many times the entire set of  $J$  diffraction patterns is processed through the algorithm.



The use of an autograd environment allows to easily experiment with the batch-size parameters: EPIE and DM are completely antipodal in this sense, as the first is a sequential algorithm (stochastic gradient descent), while the second employs all the measured data at once (gradient descent). The batch size hyper-parameter allows to span between the two worlds. Within this framework, new first-order optimisers such as Adam<sup>42</sup> become readily available, providing a considerable acceleration to the plain old gradient descent method described by (4).

#### 4.1 Experiments on synthetic data

To investigate the effects of our correction routine, for each dataset the propagation distance is initialised to a value corrupted by a 30% error, while each position is perturbed by a random jitter with a standard deviation of 10 pixels. Both the propagation distance and the position vectors are added to the optimisation pool. Apart from eye inspection, to validate the method, reconstruction quality can be analysed observing the behaviour of (I) the optimisation dissimilarity (5), calculated between the simulated and the measured diffraction pattern, and (II) a truth-aware similarity metric, SSIM<sup>39</sup>, which obviously can be applied for simulated data only. In the latter case, the positions error and the propagation distance estimate can be monitored at each iteration, producing informative graphics which are the base for the following analysis.

In the example dataset here shown (Fig. 5),  $O(\mathbf{r})$  is made by the "Pepperoni" (magnitude) and "Peaches" (phase) images, while  $P(\mathbf{r})$  is composed by the "Chelsea cat" (magnitude) and "Astronaut" (phase) pictures. It can be seen that in around 500 epochs both the positions and the distance have recovered more than 90% of initial error, producing the object and illumination estimate which can be seen in Fig. 7. The dissimilarity error (leftmost panel in Fig. 5) is used as the guiding metrics to optimise the object, the illumination and the setup parameters. The use of the grid sampler is essential to increase the convergence, which tends to be slower for the case of optimisation-like reconstruction algorithm based on the a typical crop operator; the effect can be traced back to the inherent regularisation action of the interpolator.

In the uppermost panel of Fig. 6, the distribution of the position error is shown for each epoch, denoting a Rayleigh-like distribution, which tends to be narrower as the epochs increase; the median, indeed decay towards 0, indicating a good correction. The desired single-modality form of the distribution is an effect of a refined version of the problem expression: we have to optimise only additive correction factors for the positions, not just the positions. In this manner, an  $L_1$  metric can be used to create a regularisation term on these correction factors.

Fig. 8 panel A shows how during the reconstruction the SSIM increases as the propagation distance (panel A) approaches the correct value. Each color is relative to a different datasets. The longest trails are the one for which the propagation distance is larger, then the optimisation, initialised with a 30% error, spans for an extended range of  $z$ . Conversely, for small propagation distances, the regression of the correct value tends to be faster. Panel B shows a similar graph but for the positions' error median: here the behaviour is more chaotic and not so dependent on the propagation distance error. Convergence speed in the various phases can be guessed by observing the sparsity of the points for each error value.

#### 4.2 Soft-X-rays experiment

In this section, reconstructions obtained from a soft X-ray experiment are presented. The imaging experiment has been performed at the TwinMic spectromicroscopy beamline<sup>52,53</sup> at the Elettra synchrotron facility. TwinMic can operate in three imaging modalities: I) STXM; II) full-field TXM/CDI; III) scanning CDI (ptychography). Clearly the latter (the one used for this work) is obtained by combining the optic setup of the second modality and the control of the sample stage from the first one.

Similarly to other ptychography experiments performed at the beamline (e.g. <sup>16,17,54</sup>), X-ray data were collected using a 1020 eV X-ray synchrotron beam<sup>52</sup> focused with a 600 um diameter Fresnel zone plate (FZP) with an outer zone width of 50 nm placed approximately 2 m downstream a 25 um aperture that defines a secondary source. A Peltier-cooled charge-coupled device (CCD) detector (Princeton MT-MTE) with 1300x1340 20x20 um square pixels was placed roughly 72 cm downstream of the FZP. According to Abbe theory<sup>16</sup>, the limit of resolution for coherent illumination is  $\Gamma = 0.82\lambda/NA = 50$  nm. The resolution in Fresnel CDI is a function of the experimental geometry<sup>55</sup>, namely the distance from the focal point of the FZP to the detector and the physical size of the detector itself, rather than the focusing optics. The scan pattern used for the acquisition is shown in figure 10.

From the ptychography configuration point of view, the situation is similar to the one presented in<sup>56</sup>, where a point source (obtained by idealising the focus of an FZP through an Order Sorting Aperture) illuminates the sample. Following the approach of<sup>56</sup>, during the data analysis the beam has been parallelized by using the Fresnel Scaling Theorem<sup>48</sup>. In the following experiment, as pointed out in section 2, the sample is considered sufficiently thin<sup>22,57</sup> to be modelled by a multiplicative complex transmission function  $h$  defined by the expression

$$h(\mathbf{r}) = e^{j\frac{2\pi}{\lambda}[n(\mathbf{r})-1]t(\mathbf{r})} = e^{j\frac{2\pi}{\lambda}t(\mathbf{r})[-\delta(\mathbf{r})+j\beta(\mathbf{r})]} \quad (13)$$

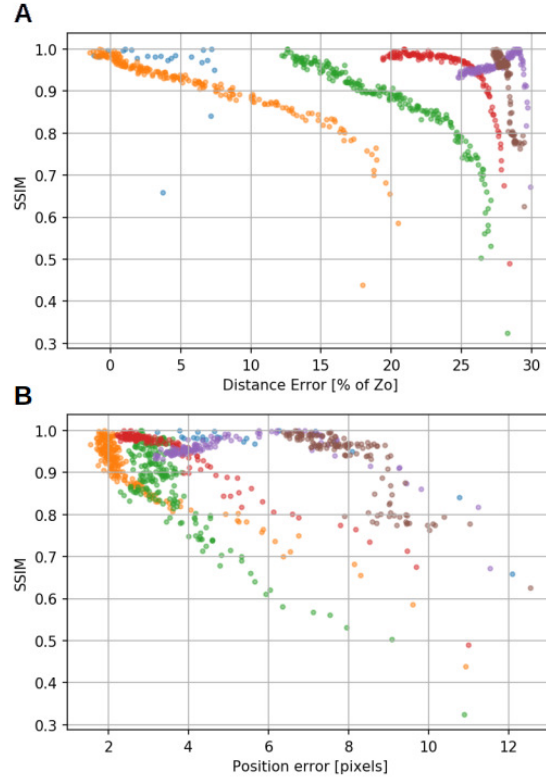


**Figure 8.** Normalised SSIM as a function of the propagation distance error (panel A) and the median of the scan positions error (panel B), calculated as the reconstruction progresses for many dataset (different colours). Convergence speed in the various phases can be guessed by observing the sparsity of the points for each error value.

where  $\mathbf{r}$  is the planar coordinate on the sample plane,  $n(\mathbf{r})$  is the complex refractive index and  $t(\mathbf{r})$  a real  $R^2 \mapsto R^1$  function defining the local thickness. From the reconstruction-inferred  $h(\mathbf{r})$  (the objective of the reconstruction), the magnitude map corresponds to:

$$\ln |h(\mathbf{r})| = \ln \sqrt{I(\mathbf{r})} = \ln \sqrt{I_o(\mathbf{r})} - \frac{2\pi}{\lambda} \beta(\mathbf{r}) \cdot t(\mathbf{r}) \quad (14)$$

where  $I_o$  is the flat field intensity and  $I$  the sample intensity. The phase map instead corresponds to:

$$\arg\{h(\mathbf{r})\} = \phi(\mathbf{r}) = -\frac{2\pi}{\lambda} \delta(\mathbf{r}) \cdot t(\mathbf{r}). \quad (15)$$

If the properties of the material ( $\beta$  and  $\delta$ ) are known, it is simple to infer its thickness and vice versa.

Diffraction data are acquired in the form of a 16-bit multi-page tiff file. The nominal positions are directly acquired from the shift vectors provided to the control system of the mechanical stage. A series of dark field images is acquired for the dark field correction.

Figure 9 shows a group of chemically fixed mesothelial cells: Mesenchymal–Epithelial Transition (MET) cells were grown on silicon nitride windows and were exposed to asbestos fibres. The absorbing diagonal bar is indeed an asbestos fibre included in the sample. The reconstructed sample is shown in magnitude (second columns) and phase (third column), where the first and the fourth ones are magnification of the red (magnitude) and green (phase) area denoted in the figure. Each row shows the reconstruction obtained with a different algorithm (multi-mode DM, multi-mode EPIE, single-mode RPIE, the proposed method "ScicComPty autodiff"). Due to the fact that for each algorithm lots of iteration (10000) are needed for this dataset, in order to reduce the computation time each diffraction pattern has been scaled to 256x256 pixels, giving a resulting pixel size of roughly 45 nm ( $\sim 5 \times 9 \text{ nm} = 45 \text{ nm}$ ) on a 846x847 pixel reconstructed image. As in all the simulated experiments, for each

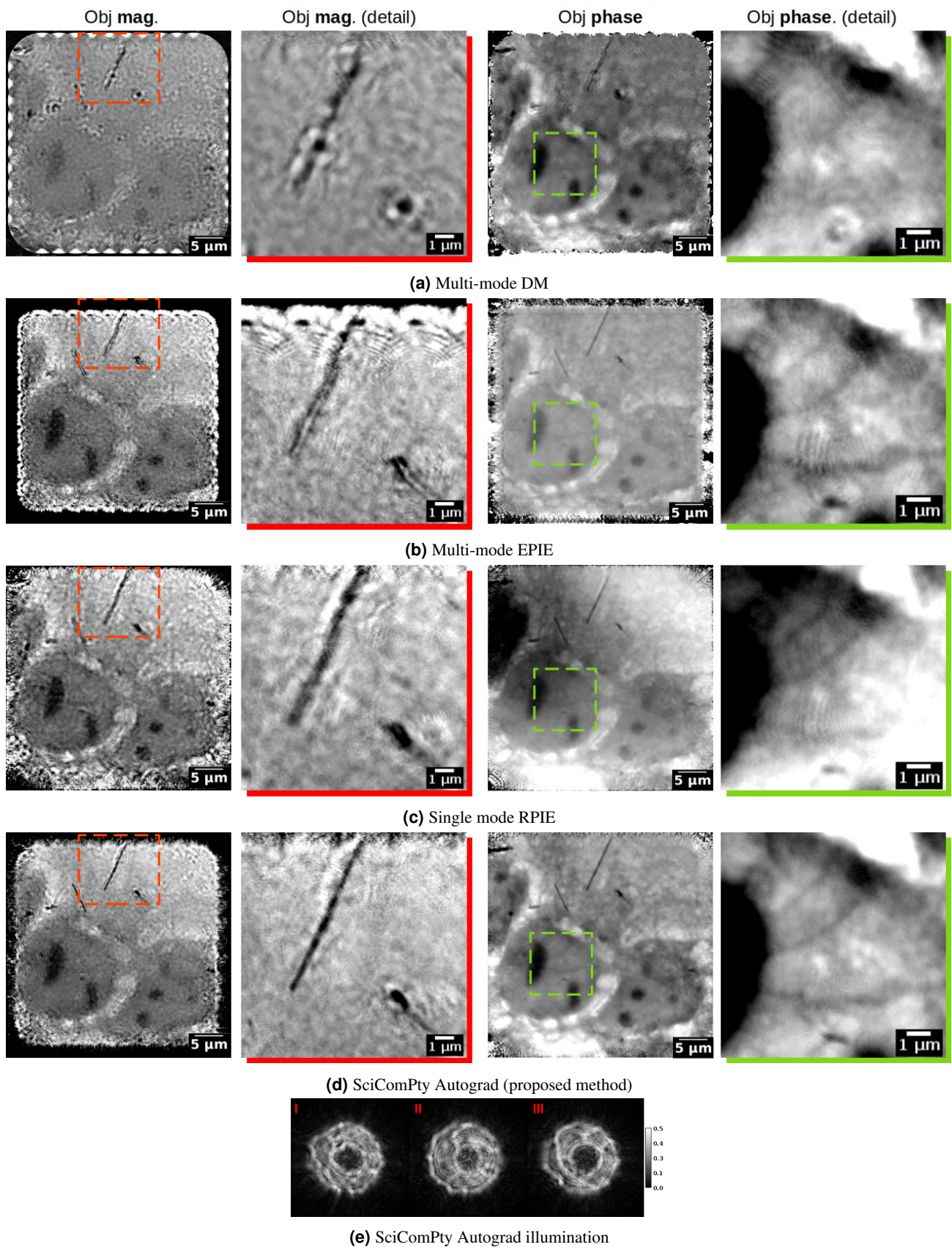


**Figure 9.** Ptychography reconstructions of MET cells exposed to asbestos: the proposed algorithm (panel d) provides the sharpest reconstruction, as can be seen from the insets. Panel e shows the retrieved multi-mode illumination.

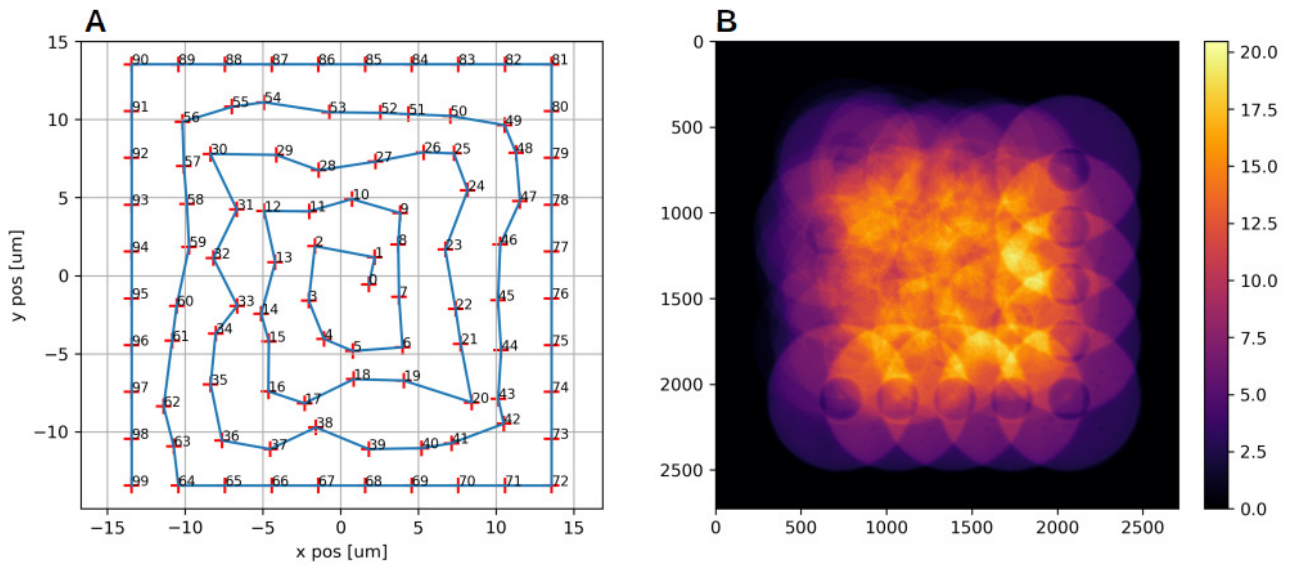


**Figure 10.** Panel A shows the final scan positions in micrometres. The corresponding sample density mask<sup>18</sup> is represented in panel B, which denotes a high sampling density especially in the center (higher overlap).

diffraction pattern the correct value of the padding is inferred by the propagation routine taking into account the wavelength and the current propagation distance value.

For many biological specimens, the phase reconstruction typically appears to be an easier problem than the correct magnitude reconstruction, as can also be seen in many published works (e.g. in<sup>35</sup>), so that one of the main indicators that the reconstruction is proceeding well is the evolution of the magnitude.

Observing the quality of the results, the proposed method (Fig. 9d) clearly surpasses all the aforementioned ones: figure 9 shows the red insets of the top left fibre, that is correctly reconstructed with the highest resolution only by the proposed algorithm; in a multi-mode DM and EPIE reconstruction lots of ringing artifacts are visible. RPIE<sup>58</sup> provides the best result among the typical reconstruction algorithms, with an object with a large field of view, which extends also in sparse sampled areas. The proposed method (fourth row) reconstructs the fiber and the cell at the highest resolution in both magnitude and phase (see Fig. 11). A second inset (green color) shows a texture in the phase reconstruction, where again the proposed method outperforms the others; cell structures are corrupted by fewer artifacts and are visible in their entire length.

The higher reconstruction quality can be attributed to the combined action of the corrections employed, e.g the automatic inference of a virtual propagation distance (Fresnel Scaling Theorem) of 0.24 mm instead of the 0.37 mm as obtained by an exhaustive manual search for the other algorithms, and the use of an advanced optimisation algorithm (Adam) in which the choice of a batch size represents a new hyperparameter that can be tuned in grain steps (then easily).

The downscaling is required not only for speed reasons, but also due to the high GPU memory consumption, which is currently a drawback of the method: as the gradient are calculated per-batch, increasing the batch size produce faster computation (less gradients are calculated for the entire set of diffraction patterns) but the memory consumption is greatly increased.

The proposed method thus provides a good reconstruction of both the magnitude and phase of the object transmission function. Figure 11 shows the line profile for each magnitude reconstruction with a FWHM resolution that is clearly twice better than the other methods.

## 5 Conclusions

In this paper, an optimisation based ptychography reconstruction algorithm is presented, which refines at the same time for the object and the setup related quantities thus proposing a solution for partial coherence, position errors and sensitivity to setup incoherences. This kind of automatic refinement not only allows to improve the viability of a ptychography experiment, but it is particularly crucial to reduce the time for a reliable analysis, which currently is highly hand-tuned. Extended tests are performed on synthetic datasets and on a real soft-X-ray dataset acquired at the Elettra TwinMic spectromicroscopy beamline, resulting in a well noticeable quality increase. We implemented our algorithm in our modular ptychography software framework, SciComPty, which is provided to the research community as open-source.



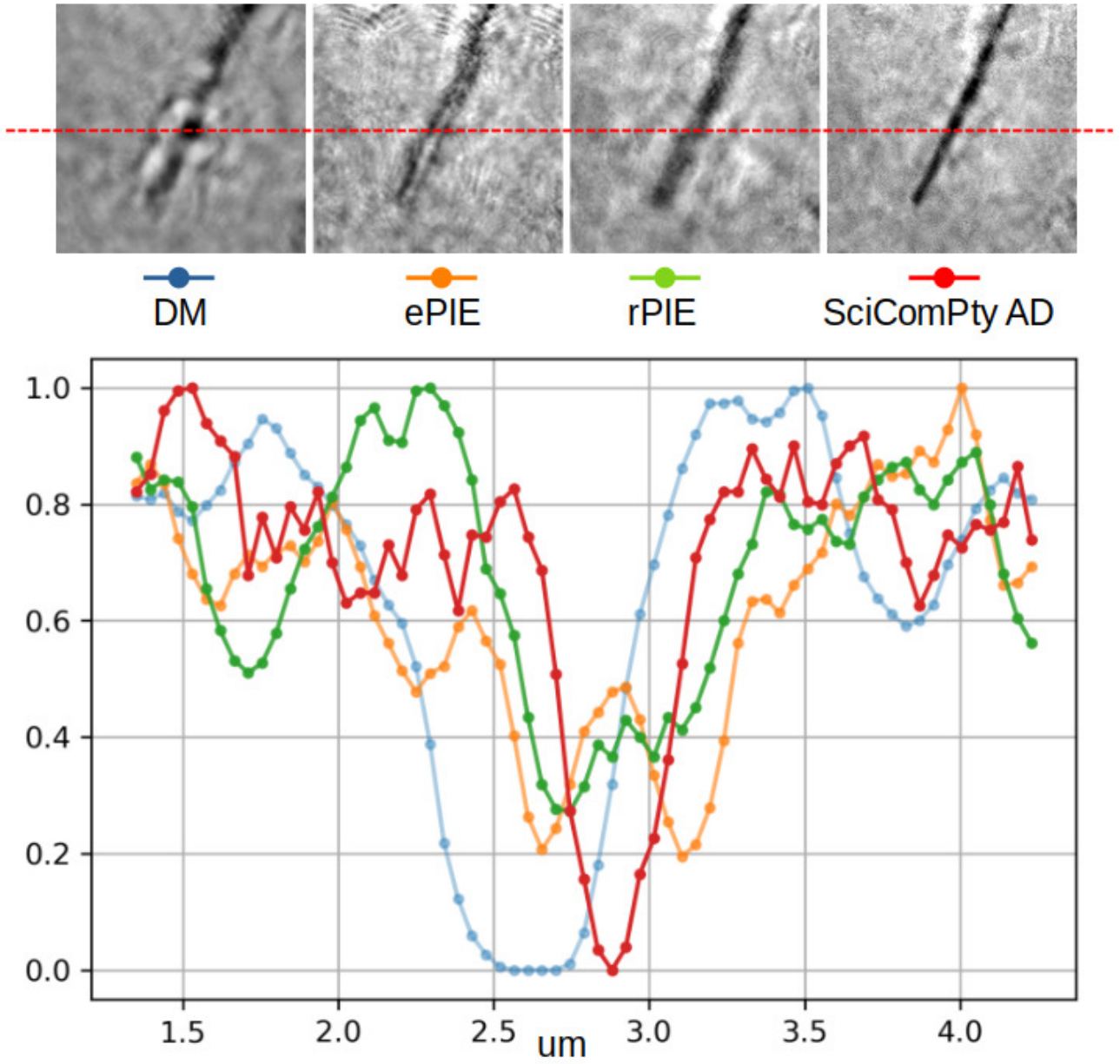


Figure 11. Line profile for each of the reconstruction in Fig. 9



## Acknowledgements

We are grateful to Roberto Borghes for its fundamental work on the TwinMic microscope control system and to Simone Sala, Gianluca Gariani and Valentina Bonanni for assistance during the beamtimes. This research has been partially developed under the Advanced Integrated Imaging Initiative (AI3); project P2017004 of Elettra Sincrotrone Trieste in agreement with University of Trieste. TwinMic (Elettra) 20185330 and 20195491 beamtimes are acknowledged.

## References

1. Paganin, D. M. & Pelliccia, D. Tutorials on x-ray phase contrast imaging: Some fundamentals and some conjectures on future developments. arXiv: 1902.00364 (2019).
2. Pfeiffer, F. X-ray ptychography. *Nat. Photonics* **12**, 9–17, DOI: [10.1038/s41566-017-0072-5](https://doi.org/10.1038/s41566-017-0072-5) (2018).
3. Guzzi, F. *et al.* A modular software framework for the design and implementation of ptychography algorithms. Submitted.
4. Vogel, C. R. *Computational Methods for Inverse Problems* (Society for Industrial and Applied Mathematics, Philadelphia, PA, USA, 2002).
5. Shechtman, Y. *et al.* Phase retrieval with application to optical imaging: A contemporary overview. *IEEE Signal Process. Mag.* **32**, 87–109, DOI: [10.1109/MSP.2014.2352673](https://doi.org/10.1109/MSP.2014.2352673) (2015).
6. Rodenburg, J. & Maiden, A. *Ptychography*, 819–904 (Springer International Publishing, Cham, 2019).
7. Hue, F., Rodenburg, J., Maiden, A. & Midgley, P. Extended ptychography in the transmission electron microscope: Possibilities and limitations. *Ultramicroscopy* **111**, 1117 – 1123, DOI: <https://doi.org/10.1016/j.ultramic.2011.02.005> (2011).
8. Shenfield, A. & Rodenburg, J. M. Evolutionary determination of experimental parameters for ptychographical imaging. *J. Appl. Phys.* **109**, 124510, DOI: [10.1063/1.3600235](https://doi.org/10.1063/1.3600235) (2011). <https://doi.org/10.1063/1.3600235>.
9. Nikolic, B. Acceleration of non-linear minimisation with PyTorch. arXiv: 1805.07439 (2018).
10. Li, T.-M., Gharbi, M., Adams, A., Durand, F. & Ragan-Kelley, J. Differentiable programming for image processing and deep learning in halide. *ACM Trans. Graph.* **37**, DOI: [10.1145/3197517.3201383](https://doi.org/10.1145/3197517.3201383) (2018).
11. Jiang, S., Guo, K., Liao, J. & Zheng, G. Solving Fourier ptychographic imaging problems via neural network modeling and tensorflow. *Biomed. Opt. Express* **9**, 3306–3319, DOI: [10.1364/BOE.9.003306](https://doi.org/10.1364/BOE.9.003306) (2018).
12. Kandel, S. *et al.* Using automatic differentiation as a general framework for ptychographic reconstruction. *Opt. Express* **27**, 18653–18672, DOI: [10.1364/OE.27.018653](https://doi.org/10.1364/OE.27.018653) (2019).
13. Schmidt, J. D. *Numerical simulation of optical wave propagation with examples in MATLAB* (SPIE, Bellingham, Washington, 2010).
14. W, G. J. *Introduction to Fourier optics, 3rd ed* (W.H.Freeman and Co Ltd, USA, 2005).
15. Guzzi, F., Kourousias, G., Bille, F., Pugliese, R. & Gianoncelli, A. Scicompty github page. <https://github.com/ElettraSciComp/SciComPty/> (2021). [Online; accessed 15-February-2021].
16. Jones, M. W. *et al.* Phase-diverse fresnel coherent diffractive imaging of malaria parasite-infected red blood cells in the water window. *Opt. Express* **21**, 32151–32159, DOI: [10.1364/OE.21.032151](https://doi.org/10.1364/OE.21.032151) (2013).
17. Kourousias, G. *et al.* Shedding light on electrodeposition dynamics tracked in situ via soft X-ray coherent diffraction imaging. *Nano Res.* **9**, 2046–2056, DOI: [10.1007/s12274-016-1095-9](https://doi.org/10.1007/s12274-016-1095-9) (2016).
18. Kourousias, G. *et al.* Monitoring dynamic electrochemical processes with in situ ptychography. *Appl. Nanosci.* **8**, 627–636, DOI: [10.1007/s13204-018-0703-2](https://doi.org/10.1007/s13204-018-0703-2) (2018).
19. Williams, G. J., Quiney, H. M., Peele, A. G. & Nugent, K. A. Fresnel coherent diffractive imaging: treatment and analysis of data. *New J. Phys.* **12**, 035020, DOI: [10.1088/1367-2630/12/3/035020](https://doi.org/10.1088/1367-2630/12/3/035020) (2010).
20. Williams, G. J. *et al.* Fresnel coherent diffractive imaging. *Phys. Rev. Lett.* **97**, 025506, DOI: [10.1103/PhysRevLett.97.025506](https://doi.org/10.1103/PhysRevLett.97.025506) (2006).
21. Maiden, A., Humphry, M., Sarahan, M., Kraus, B. & Rodenburg, J. An annealing algorithm to correct positioning errors in ptychography. *Ultramicroscopy* **120**, 64 – 72, DOI: <https://doi.org/10.1016/j.ultramic.2012.06.001> (2012).
22. Thibault, P. *et al.* High-resolution scanning x-ray diffraction microscopy. *Science* **321**, 379–382, DOI: [10.1126/science.1158573](https://doi.org/10.1126/science.1158573) (2008). <https://science.sciencemag.org/content/321/5887/379.full.pdf>.

23. Whitehead, L. W. *et al.* Diffractive imaging using partially coherent x rays. *Phys. Rev. Lett.* **103**, 243902, DOI: [10.1103/PhysRevLett.103.243902](https://doi.org/10.1103/PhysRevLett.103.243902) (2009).
24. Chen, B. *et al.* Diffraction imaging: The limits of partial coherence. *Phys. Rev. B* **86**, 235401, DOI: [10.1103/PhysRevB.86.235401](https://doi.org/10.1103/PhysRevB.86.235401) (2012).
25. Thibault, P. & Menzel, A. Reconstructing state mixtures from diffraction measurements. *Nature* **494**, 68–71, DOI: [10.1038/nature11806](https://doi.org/10.1038/nature11806) (2013).
26. Batey, D. J., Claus, D. & Rodenburg, J. M. Information multiplexing in ptychography. *Ultramicroscopy* **138**, 13 – 21, DOI: <https://doi.org/10.1016/j.ultramic.2013.12.003> (2014).
27. Li, P., Edo, T., Batey, D., Rodenburg, J. & Maiden, A. Breaking ambiguities in mixed state ptychography. *Opt. Express* **24**, 9038–9052, DOI: [10.1364/OE.24.009038](https://doi.org/10.1364/OE.24.009038) (2016).
28. Shi, X., Burdet, N., Batey, D. & Robinson, I. Multi-modal ptychography: Recent developments and applications. *Appl. Sci.* **8**, DOI: [10.3390/app8071054](https://doi.org/10.3390/app8071054) (2018).
29. Maiden, A. M. & Rodenburg, J. M. An improved ptychographical phase retrieval algorithm for diffractive imaging. *Ultramicroscopy* **109**, 1256–1262, DOI: [10.1016/j.ultramic.2009.05.012](https://doi.org/10.1016/j.ultramic.2009.05.012) (2009).
30. Lötgering, L. *et al.* Correction of axial position uncertainty and systematic detector errors in ptychographic diffraction imaging. *Opt. Eng.* **57**, 1 – 7, DOI: [10.1117/1.OE.57.8.084106](https://doi.org/10.1117/1.OE.57.8.084106) (2018).
31. Seifert, J., Bouchet, D., Loetgering, L. & Mosk, A. P. Efficient and flexible approach to ptychography using an optimization framework based on automatic differentiation. *OSA Continuum* **4**, 121–128, DOI: [10.1364/OSAC.411174](https://doi.org/10.1364/OSAC.411174) (2021).
32. Guarnieri, G., Fontani, M., Guzzi, F., Carrato, S. & Jerian, M. Perspective registration and multi-frame super-resolution of license plates in surveillance videos. *Forensic Sci. Int. Digit. Investig.* **36**, 301087, DOI: <https://doi.org/10.1016/j.fsidi.2020.301087> (2021).
33. Guizar-Sicairos, M. & Fienup, J. R. Phase retrieval with transverse translation diversity: a nonlinear optimization approach. *Opt. Express* **16**, 7264–7278, DOI: [10.1364/OE.16.007264](https://doi.org/10.1364/OE.16.007264) (2008).
34. Thibault, P. & Guizar-Sicairos, M. Maximum-likelihood refinement for coherent diffractive imaging. *New J. Phys.* **14**, 063004, DOI: [10.1088/1367-2630/14/6/063004](https://doi.org/10.1088/1367-2630/14/6/063004) (2012).
35. Mandula, O., Elzo Aizarna, M., Eymery, J., Burghammer, M. & Favre-Nicolin, V. *PyNX.Ptycho*: a computing library for X-ray coherent diffraction imaging of nanostructures. *J. Appl. Crystallogr.* **49**, 1842–1848, DOI: [10.1107/S1600576716012279](https://doi.org/10.1107/S1600576716012279) (2016).
36. Powell, M. J. D. An efficient method for finding the minimum of a function of several variables without calculating derivatives. *The Comput. J.* **7**, 155–162, DOI: [10.1093/comjnl/7.2.155](https://doi.org/10.1093/comjnl/7.2.155) (1964). <https://academic.oup.com/comjnl/article-pdf/7/2/155/959784/070155.pdf>.
37. Tripathi, A., McNulty, I. & Shpyrko, O. G. Ptychographic overlap constraint errors and the limits of their numerical recovery using conjugate gradient descent methods. *Opt. Express* **22**, 1452–1466, DOI: [10.1364/OE.22.001452](https://doi.org/10.1364/OE.22.001452) (2014).
38. Guzzi, F. *et al.* Refining scan positions in ptychography through error minimisation and potential application of machine learning. *J. Instrumentation* **13**, C06002–C06002, DOI: [10.1088/1748-0221/13/06/c06002](https://doi.org/10.1088/1748-0221/13/06/c06002) (2018).
39. Zhou Wang, Bovik, A. C., Sheikh, H. R. & Simoncelli, E. P. Image quality assessment: from error visibility to structural similarity. *IEEE Transactions on Image Process.* **13**, 600–612, DOI: [10.1109/TIP.2003.819861](https://doi.org/10.1109/TIP.2003.819861) (2004).
40. Dwivedi, P., Konijnenberg, A., Pereira, S. & Urbach, H. Lateral position correction in ptychography using the gradient of intensity patterns. *Ultramicroscopy* **192**, 29 – 36, DOI: <https://doi.org/10.1016/j.ultramic.2018.04.004> (2018).
41. Zhang, F. *et al.* Translation position determination in ptychographic coherent diffraction imaging. *Opt. Express* **21**, 13592–13606, DOI: [10.1364/OE.21.013592](https://doi.org/10.1364/OE.21.013592) (2013).
42. Kingma, D. P. & Ba, J. Adam: A method for stochastic optimization. In Bengio, Y. & LeCun, Y. (eds.) *3rd International Conference on Learning Representations, ICLR 2015, San Diego, CA, USA, May 7-9, 2015, Conference Track Proceedings* (2015).
43. Gürsoy, D. *et al.* Rapid alignment of nanotomography data using joint iterative reconstruction and reprojection. *Sci. Reports* **7**, 11818, DOI: [10.1038/s41598-017-12141-9](https://doi.org/10.1038/s41598-017-12141-9) (2017).
44. Bartholomew-Biggs, M., Brown, S., Christianson, B. & Dixon, L. Automatic differentiation of algorithms. *J. Comput. Appl. Math.* **124**, 171 – 190, DOI: [https://doi.org/10.1016/S0377-0427\(00\)00422-2](https://doi.org/10.1016/S0377-0427(00)00422-2) (2000). Numerical Analysis 2000. Vol. IV: Optimization and Nonlinear Equations.

45. Baydin, A. G., Pearlmutter, B. A., Radul, A. A. & Siskind, J. M. Automatic differentiation in machine learning: a survey. *J. Mach. Learn. Res.* **18**, 153:1–153:43 (2017).
46. van Merriënboer, B., Breuleux, O., Bergeron, A. & Lamblin, P. Automatic differentiation in ML: where we are and where we should be going. In Bengio, S. *et al.* (eds.) *Advances in Neural Information Processing Systems 31: Annual Conference on Neural Information Processing Systems 2018, NeurIPS 2018, December 3-8, 2018, Montréal, Canada*, 8771–8781 (2018).
47. Paszke, A. *et al.* Pytorch: An imperative style, high-performance deep learning library. In Wallach, H. M. *et al.* (eds.) *Advances in Neural Information Processing Systems 32: NeurIPS 2019, December 8-14, 2019, Vancouver, BC, Canada*, 8024–8035 (2019).
48. Paganin, D. *Coherent X-ray Optics* (Oxford University Press, Oxford, 2006).
49. Fischer, R. F. H. *Precoding and Signal Shaping for Digital Transmission* (John Wiley and Sons, Chicago, 2002).
50. Jaderberg, M., Simonyan, K., Zisserman, A. & Kavukcuoglu, K. Spatial transformer networks. In Cortes, C., Lawrence, N. D., Lee, D. D., Sugiyama, M. & Garnett, R. (eds.) *Advances in Neural Information Processing Systems 28: Annual Conference on Neural Information Processing Systems 2015, December 7-12, 2015, Montreal, Quebec, Canada*, 2017–2025 (2015).
51. Guzzi, F. *et al.* Distillation of an end-to-end oracle for face verification and recognition sensors. *Sensors* **20**, DOI: [10.3390/s20051369](https://doi.org/10.3390/s20051369) (2020).
52. Gianoncelli, A., Kourousias, G., Merolle, L., Altissimo, M. & Bianco, A. Current status of the TwinMic beamline at Elettra: a soft X-ray transmission and emission microscopy station. *J. Synchrotron Radiat.* **23**, 1526–1537, DOI: [10.1107/S1600577516014405](https://doi.org/10.1107/S1600577516014405) (2016).
53. Malucelli, E. *et al.* X-ray fluorescence microscopy of light elements in cells: self-absorption correction by integration of compositional and morphological measurements. *J. Physics: Conf. Ser.* **463**, 012022, DOI: [10.1088/1742-6596/463/1/012022](https://doi.org/10.1088/1742-6596/463/1/012022) (2013).
54. Bozzini, B. *et al.* Soft x-ray ptychography as a tool for in operando morphochemical studies of electrodeposition processes with nanometric lateral resolution. *J. Electron Spectrosc. Relat. Phenom.* **220**, 147 – 155, DOI: <https://doi.org/10.1016/j.elspec.2017.01.004> (2017). Proceedings of the “39th International Conference on Vacuum Ultraviolet and X-ray Physics (VUVX-2016).
55. Quiney, H. Coherent diffractive imaging using short wavelength light sources. *J. Mod. Opt.* **57**, 1109–1149, DOI: [10.1080/09500340.2010.495459](https://doi.org/10.1080/09500340.2010.495459) (2010). <https://doi.org/10.1080/09500340.2010.495459>.
56. Stockmar, M. *et al.* Near-field ptychography: phase retrieval for inline holography using a structured illumination. *Sci. Reports* **3**, 1927, DOI: [10.1038/srep01927](https://doi.org/10.1038/srep01927) (2013).
57. Maiden, A. M., Humphry, M. J. & Rodenburg, J. M. Ptychographic transmission microscopy in three dimensions using a multi-slice approach. *J. Opt. Soc. Am. A* **29**, 1606–1614, DOI: [10.1364/JOSAA.29.001606](https://doi.org/10.1364/JOSAA.29.001606) (2012).
58. Maiden, A., Johnson, D. & Li, P. Further improvements to the ptychographical iterative engine. *Optica* **4**, 736–745, DOI: [10.1364/OPTICA.4.000736](https://doi.org/10.1364/OPTICA.4.000736) (2017).